

A Probabilistic Model for Image Processing with Positivity Constraint and Spectral Density Control

Pierre Minier^{*}

Jean-François Giovannelli^{*}

François Orieux[†]

^{*}IMS (Univ. Bordeaux – CNRS – BINP)

[†]L2S (Univ. Paris-Saclay – CNRS – CentraleSupélec)

Abstract—This paper introduces a novel probabilistic model for images that addresses the challenge of simultaneously (1) maintaining pixel value positivity, (2) controlling the Power Spectral Density, and (3) ensuring an explicit partition function. This work serves as a preliminary step toward a fully self-supervised image deconvolution technique with these properties. The approach leverages a white positive field and introduces correlation through a filtering preserving the positivity. An example featuring an auto-regressive filter and a truncated normal distribution is developed. To facilitate parameter estimation and model manipulation, the probability density function of the resulting field is derived in the Fourier domain. A detailed analysis of the positivity constraint is also provided based on this example. Additionally, a Random Walk Metropolis sampler is proposed, with two complete parameter estimation examples: one using synthetic image data and the other based on real-world image data.

Index Terms—Positivity Constraint, Power Spectral Density, Partition Function, Image, Bayesian, Random Walk Metropolis

I. INTRODUCTION

This work lays the foundations for advanced, fully self-supervised image deconvolution techniques under a positivity constraint. This constraint ensures that pixel values remain physically meaningful by enforcing non-negativity. Fully self-supervised techniques aim to estimate not only the image but also instrument parameters, structural parameters, the level parameters of the object, error characteristics (e.g., correlation, PSD, texture), and other relevant hyperparameters [1]. The model is built on three key features.

1. Positivity. Ensuring positive pixel values is a critical constraint tied to physical quantities such as energy, intensity, or absolute/Kelvin temperature, leading to more physically meaningful and accurate restorations [2].

2. PSD control. The PSD encapsulates essential physical information. For instance, in astronomy, it supports tip-tilt corrections using adaptive optics [3], while in microscopy, it characterises phenomena such as speckles [4].

3. Explicit partition function. The third feature is a closed-form partition function, including hyperparameter dependencies. This feature facilitates efficient hyperparameter estimation [5] [6].

To the best of our knowledge, no existing model in the literature simultaneously offers this three features. To address

this gap, this paper introduces a novel model that is simple, practical, and innovatively leverages well-known tools such as the Fourier transform, multivariate variable changes, and filtering techniques.

Section II constructs the model, highlights its key properties, and discusses its theoretical foundations. Section III presents an illustrative example, deriving the explicit density and showcasing realisations. Section IV explores the parameter estimation framework and its implications for the posterior density and constraints. Section V provides a detailed analysis of the positivity constraint and its impact. Finally, Section VI introduces a random walk algorithm for parameter estimation, demonstrating the model’s effectiveness on both synthetic and real-world data.

II. MODEL

A. Field construction

Let P denote the number of pixels. Consider a field \mathbf{U} with independent and identically distributed components, following a probability density function f_U on \mathbb{R}_+^P . Let \mathcal{I}_+ denote the indicator function of \mathbb{R}_+^P . The components can follow various distributions, such as the Uniform on a positive segment, the Gamma [7], the Lévy [8], or the Truncated Normal [9].

To introduce correlation while maintaining positivity, one can multiply \mathbf{U} by a matrix \mathbf{A}_ω with positive entries. For a realisation \mathbf{u} , a corresponding \mathbf{x} of \mathbf{X} is obtained

$$\mathbf{x} = \mathbf{A}_\omega \mathbf{u}. \quad (1)$$

The parameter ω acts as a shape factor (or a set of related factors) and will be detailed later.

Let us consider \mathbf{A}_ω invertible. Using the change of variables formula [10], one obtains the explicit density $f_{X|H}$ of \mathbf{X}

$$f_{X|H}(\mathbf{x}|\boldsymbol{\eta}) = |\det \mathbf{A}_\omega|^{-1} f_U(\mathbf{A}_\omega^{-1} \mathbf{x}) \mathcal{I}_+(\mathbf{A}_\omega^{-1} \mathbf{x}) \quad (2)$$

with $\boldsymbol{\eta}$ encompassing the parameters of \mathbf{U} and ω .

To exploit this model: (i) \mathbf{A}_ω represents a circulant convolution; and (ii) \mathbf{U} has first and second moments. Although our application focuses on images, the model is not limited to them. Also, \mathbf{A}_ω can be chosen to be diagonalised by the DCT or DST, depending on the choice of boundary conditions [11].

B. Diagonalisation in the Fourier Domain

\mathbf{A}_ω is Circulant Block Circulant [12], and can be rewritten

$$\mathbf{A}_\omega = \mathbf{F}^{-1} \boldsymbol{\Lambda}_\omega \mathbf{F} \quad (3)$$

This work was supported by a French government grant managed by the Agence Nationale de la Recherche under the France 2030 program, reference ANR-22-EXOR-0016, by the University of Bordeaux with the RRI ORIGINS, and by the Region Nouvelle Aquitaine.

where \mathbf{F} is the discrete Fourier transform matrix. The diagonal matrix $\mathbf{\Lambda}_\omega$ contains the discretised frequency responses noted as $\lambda_\omega(p)$. We then have

$$\begin{aligned}\mathbf{\Lambda}_\omega &= \mathbf{F}\mathbf{A}_\omega\mathbf{F}^{-1} = \text{diag}[\lambda_\omega(p), p = 0, \dots, P-1], \\ \hat{\mathbf{x}} &= \mathbf{F}\mathbf{x} = \mathbf{F}\mathbf{A}_\omega\mathbf{u} = \mathbf{F}\mathbf{F}^{-1}\mathbf{\Lambda}_\omega\mathbf{F}\mathbf{u} = \mathbf{\Lambda}_\omega\mathbf{F}\mathbf{u} = \mathbf{\Lambda}_\omega\hat{\mathbf{u}},\end{aligned}\quad (4)$$

where $\hat{\mathbf{x}}$ and $\hat{\mathbf{u}}$ are the Fourier transforms of \mathbf{x} and \mathbf{u} .

C. Smooth images and Positivity Preservation

The filters $\mathbf{\Lambda}_\omega$ are designed to be low-pass to produce smooth images. Their frequency response (FR) is normalised to one at zero frequency to preserve the mean level μ . In short, by attenuating high-frequency components, the filters reduce the variance of \mathbf{U} and smooth out large variations, thereby ensuring the positivity of \mathbf{X} .

D. Power Spectral Density and Covariance

Let γ denote the precision of \mathbf{U} , \hat{a}_ω the continuous FR and a_ω the impulse response (IR). The PSD and the covariance of \mathbf{X} are given by

$$S_x(\nu_h, \nu_v) = \gamma^{-1} |\hat{a}_\omega(\nu_h, \nu_v)|^2 \quad (5)$$

$$C_x(n_h, n_v) = \gamma^{-1} a_\omega(n_h, n_v) \otimes a_\omega(-n_h, -n_v) \quad (6)$$

with \otimes the 2D convolution operator.

III. EXAMPLE

A. Filter

The chosen FR (7) is parameterised by $\omega \in]-1, 1[$, which describes the bandwidth and thus the level of correlation.

$$\hat{a}_\omega(\nu_h, \nu_v) = \frac{1 - \omega}{\sqrt{1 + \omega^2 - 2\omega \cos(2\pi\sqrt{\nu_h^2 + \nu_v^2})}} \quad (7)$$

It is designed with circular symmetry around the zero frequency.

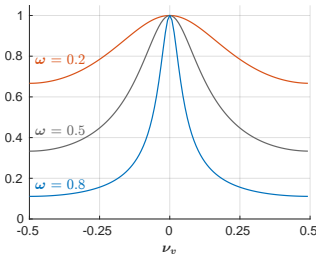


Fig. 1: FR at $\nu_h = 0$ with different correlations ω .

Fig. 1 shows a cross-section for different values of ω . For $\omega > 0$, the filter behaves as a low-pass filter, meaning that higher frequencies are attenuated compared to lower ones. As ω increases towards one, the image becomes smoother. Therefore, the interval $[0, 1]$ represents the a priori range.

B. Density of the white field

The components of \mathbf{U} follow a Truncated Normal distribution at zero [9]. While truncation modifies the partition function, it remains analytically known (9). Here $\boldsymbol{\eta} = [\mu, \gamma, \omega]$.

$$f_U(\mathbf{u}) = K(\boldsymbol{\eta})^P \exp\left(-\frac{\gamma}{2}\|\mathbf{u} - \mu\mathbf{1}\|^2\right) \mathcal{I}_+(\mathbf{u}) \quad (8)$$

$$K(\boldsymbol{\eta}) = \sqrt{\frac{\gamma}{2\pi}} \times \frac{2}{1 + \text{erf}\left(\mu\sqrt{\gamma/2}\right)} \quad (9)$$

For generating a sample of \mathbf{U} without numerical errors from the error function (erf), one can refer to [13] or [14].

C. Density of the correlated field

By applying the formula of variable change (2) to the density f_U (8), the density of \mathbf{X} is $f_{X|\mathbf{H}}(\mathbf{x} | \boldsymbol{\eta}) =$

$$\frac{K(\boldsymbol{\eta})^P}{|\det \mathbf{A}_\omega|} \exp\left(-\frac{\gamma}{2}\|\mathbf{A}_\omega^{-1}\mathbf{x} - \mu\mathbf{1}\|^2\right) \mathcal{I}_+(\mathbf{A}_\omega^{-1}\mathbf{x}).$$

Using (3) one can rewrite $f_{X|\mathbf{H}}(\mathbf{x} | \boldsymbol{\eta}) =$

$$\prod_{p=1}^P \frac{K(\boldsymbol{\eta})}{|\lambda_\omega(p)|} \exp\left(-\frac{\gamma}{2}\left|\frac{\hat{x}_p}{\lambda_\omega(p)} - \mu\hat{\mathbf{1}}_p\right|^2\right) \mathcal{I}_+(\mathbf{F}^{-1}\mathbf{\Lambda}_\omega^{-1}\hat{\mathbf{x}})$$

with $\hat{\mathbf{1}} = \mathbf{F}\mathbf{1}$. This expression is separable over the frequencies, except for the indicator function.

D. Realisations

For illustration, the same realisation of \mathbf{U} is used, sized (512×512) , with mean $\mu = 1$, precision $\gamma = 2$, and varying $\omega \in]0, 1[$ to represent different levels of correlation.

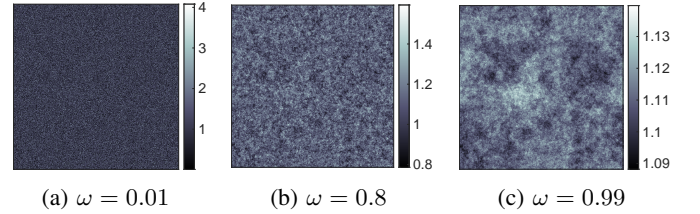


Fig. 2: Realisations of the correlated field with different ω

As ω increases, larger clusters of pixels with similar values emerge, reflecting stronger correlations due to the filter's increasingly low-pass nature. Each filtering conserves the same mean pixel level, while the colour bar ranges tighten, also a result of the filter's low-pass effect.

IV. ESTIMATION

In the following, a realisation \mathbf{x}^* of \mathbf{X} is observed. Typical examples are provided on Fig. 2. As part of a self-supervised image deconvolution technique, the vector $\boldsymbol{\eta}^*$ must be estimated and a Bayesian method is developed [15].

A. Log Posterior

The distribution of $\mathbf{H} | \mathbf{X}$ is expressed in terms of the likelihood $\mathbf{X} | \mathbf{H}$ and the prior on \mathbf{H} , which is chosen to be separable and uniform. Note that the estimation approach employed only requires knowledge of the posterior distribution up to a multiplicative constant

$$\pi_{\mathbf{H}|\mathbf{X}}(\boldsymbol{\eta} | \mathbf{x}^*) \propto f_{X|\mathbf{H}}(\mathbf{x}^* | \boldsymbol{\eta}) \pi_{\mathbf{H}}(\boldsymbol{\eta}). \quad (10)$$

The log-posterior, within the domain defined by the prior, is expressed as $LP(\boldsymbol{\eta}) \#$

$$\log \mathcal{I}_+(\mathbf{F}^{-1}\mathbf{\Lambda}_\omega^{-1}\hat{\mathbf{x}}^*) + \sum_{p=0}^{P-1} \log \frac{K(\boldsymbol{\eta})}{|\lambda_\omega(p)|} - \frac{\gamma}{2} \left| \frac{\hat{x}_p^*}{\lambda_\omega(p)} - \mu\hat{\mathbf{1}}_p \right|^2. \quad (11)$$

B. Indicator Function

The indicator $\mathcal{I}_+(\mathbf{F}^{-1}\Lambda_\omega^{-1}\hat{\mathbf{x}}^*)$ inside (11) acts on the pixel space \mathbb{R}_+^P , while also influencing ω . This can be rewritten using (4) by introducing the Fourier transform of the true \mathbf{u}^* that generated \mathbf{x}^* with the true ω^* .

$$\mathcal{I}_+(\mathbf{F}^{-1}\Lambda_\omega^{-1}\hat{\mathbf{x}}^*) = \mathcal{I}_+(\mathbf{F}^{-1}\Lambda_\omega^{-1}\Lambda_{\omega^*}\hat{\mathbf{u}}^*).$$

Qualitatively, when $\Lambda_\omega^{-1}\Lambda_{\omega^*}$ is low-pass, the positive realisation \mathbf{u}^* is spatially averaged, resulting in positive filtering. However, if $\Lambda_\omega^{-1}\Lambda_{\omega^*}$ is high-pass, the filtering increases the variance. Since the support of \mathbf{U} is bounded below by 0, negative values may occur, especially with numerous pixels. A more quantitative analysis is provided in Section V-B.

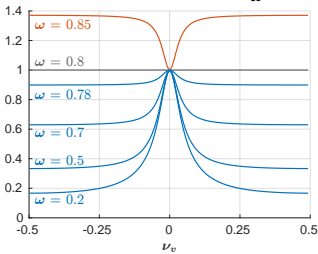


Fig. 3: FR of $\Lambda_\omega^{-1}\Lambda_{\omega^*}$ at $\nu_h = 0$ with different of ω for a given $\omega^* = 0.8$.

V. ANALYSIS OF THE CONSTRAINT

A. Conditional Densities

Using (11), Fig. 4 shows the conditional densities of two components of $\boldsymbol{\eta}$ while keeping the third fixed at its true value. These plots result from a brute-force exploration of the corresponding 2D parameter space. Red squares highlight the true $\boldsymbol{\eta}^*$ and green points the MAP, both within high-probability regions, while colourless areas represent zero-posterior zones imposed by constraints, with dashed contour lines extending these regions. It is clear that the constraint is active and depends solely on the filter parameter ω .

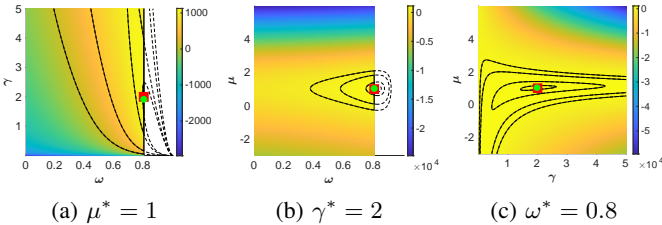


Fig. 4: Log Conditional Posterior with $\boldsymbol{\eta}^*$

B. Analysis of the constraint in one dimension

To better understand the behaviour of the constraint $\mathcal{I}_+(\mathbf{F}^{-1}\Lambda_\omega^{-1}\Lambda_{\omega^*}\hat{\mathbf{u}}^*)$, we consider the one-dimensional case :

$$\hat{a}_\omega(\nu) = \frac{1 - \omega}{\sqrt{1 + \omega^2 - 2\omega \cos(2\pi\nu)}}.$$

This FR is linked to the Z-transform $H_\omega(z) = |\hat{a}_\omega(\nu)|e^{j\varphi}$ with $z = e^{j2\pi\nu}$. We set the phase φ to zero. Recognising a geometric series, one can re-express this as

$$H_\omega(z) = \frac{1 - \omega}{1 - \omega z^{-1}} = (1 - \omega) \sum_{n=0}^{+\infty} \omega^n z^{-n}. \quad (12)$$

Thus, \mathbf{u} is low-pass filtered using the true $0 < \omega^* < 1$ by applying an autoregressive filter. The resulting signal is then processed through the inverse filter using a proposed ω .

$$G_{\omega^*, \omega}(z) = \frac{1 - \omega^*}{1 - \omega} \left[1 + \sum_{n=1}^{+\infty} (\omega^*)^{n-1} (\omega^* - \omega) z^{-n} \right]. \quad (13)$$

The IR is given by the coefficients of z^{-n} .

Based on 10,000 signal realisations of length $N = 16$ in (a) and $N = 1024$ in (b), Fig. 5 shows the empirical proportions of constraint validation in the parameter space (ω^*, ω) using the equivalent filter (13).

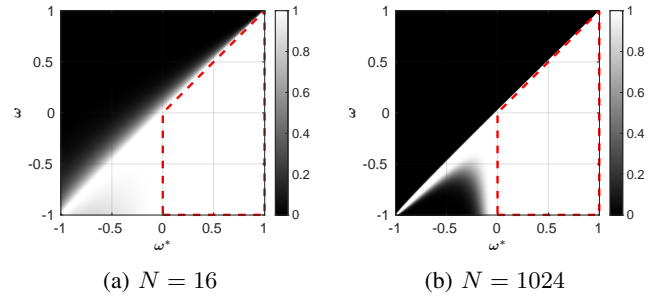


Fig. 5: Proportions of constraint validation.

An important result is the guarantee of positivity within the red dotted trapezoid. Since the IR coefficients and inputs are positive, the output is inherently positive. Also, along the diagonal $\omega = \omega^*$, the filtering is all-pass, so the output equals the positive input signal \mathbf{u} .

In other configurations, the IR is neither fully positive nor fully negative, and the filter behaves like a differentiator, reflecting a high-pass nature (e.g., $\omega = 0.85$ in Fig. 3). This reduces value concentration around the mean, extending the lower bound into negatives and losing positivity guarantees.

For large sample sizes ($N \geq 1024$), values $\omega > \omega^*$ appear to be prohibited, which is less apparent with fewer samples. For $\omega > \omega^* > 0$, only the first IR coefficient is positive, while the others are negative, increasing the likelihood of violating the constraint as N grows.

Finally, when $\omega^* < 0$, a high-pass filter is initially applied, which prevents smooth image generation. In this case, stronger inverse filtering and fewer elements are needed to meet the constraint effectively.

VI. ALGORITHM AND RESULTS

A. Random Walk Metropolis

One approach to estimate $\boldsymbol{\eta}$ is to consider the posterior mean. It is computed as the empirical mean of samples drawn from the posterior. To obtain these samples, a Random Walk Metropolis (RWM) algorithm [16] is employed. This approach provides both an estimate and a measure of uncertainty.

Algorithm 1 RWM

```

1: Set  $\eta_0$  to the MAP obtained by optimising  $\pi_{H|X}$ 
2: for  $t = 1$  to  $T$  do
3:   Sample  $\eta^p$  from  $\mathcal{N}(\eta_{t-1}, \Sigma_H)$ 
4:   Compute  $\alpha = LP(\eta^p) - LP(\eta_{t-1})$ 
5:   Sample  $r$  from Uniform(0, 1)
6:   if  $r < \alpha$  then  $\eta_t = \eta^p$ 
7:   else  $\eta_t = \eta_{t-1}$ 
8: end for

```

The Markov chain is initialised at the MAP estimate of $\pi_{H|X}$, which is computed using a coordinate-wise Golden Section Search [17]. This choice is motivated by the apparent unimodality of the posterior distribution (see Fig. 4). Starting the chain at the MAP offers two advantages: (i) it places the initial sample in a valid region of high posterior density, which promotes faster convergence, and (ii) it enables a direct comparison between the MAP estimate and the posterior mean.

B. Synthetic data

Fig. 6 illustrates an example of MAP estimate and MCMC chains obtained. Repeated experiments yield highly similar results. The estimation accuracy improves with the number of pixels. For a synthetic image of size (512×512) , the resulting estimates are :

η	True	MAP	Mean \pm Std
μ	1	1.000	$1.000 \pm 2e-3$
γ	2	1.998	$1.999 \pm 6e-3$
η	0.8	0.800002	$0.800004 \pm 3e-6$

The ω samples reach a constraint limit, consistent with the analysis in V-B and the posteriors in Fig. 4. This limit is close to, but distinct from, the true value, the MAP estimate, and the empirical mean.

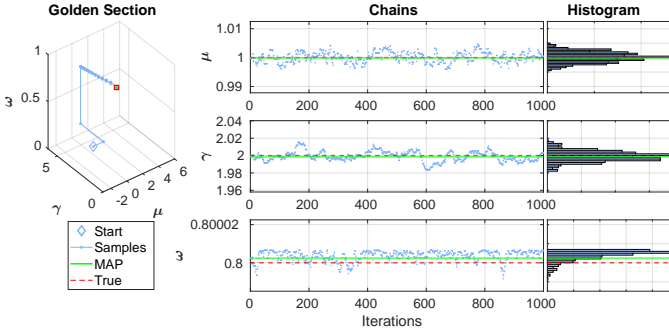


Fig. 6: MAP, chains and histograms on synthetic data.

Regarding computation time, MAP estimation took 5.2 s with 1760 log-posterior evaluations, reaching an accuracy of about 10^{-3} for all components of η . MCMC sampling required 2.6 s for 1000 evaluations, with an acceptance rate of 48%.

C. Real-world data

We use a 512×512 crop of the Horsehead Nebula from the Callisto telescope at the SSO Observatory in 2018 [18],

presented on Fig. 7. Since this is real-world data, the true η^* is unavailable. We use the same prior intervals for μ , γ , and

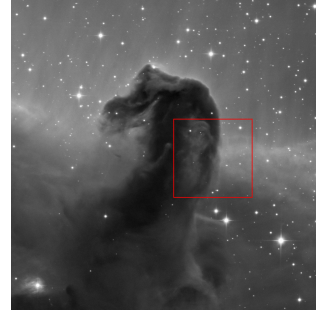


Fig. 7: The 512×512 crop is outlined by the red square.

ω , as well as the same step size as for the synthetic data. Both MAP estimation and MCMC converge faster, requiring around 3 s in total, as confirmed by repeated runs. The tight posteriors in the histograms highlight the model's relevance for real data. The acceptance rate remains similar, at 43%. Results are provided on the following table and on Fig. 8.

η	MAP	Mean \pm Std
μ	1.939	$1.938 \pm 2e-3$
γ	0.834	$0.834 \pm 3e-3$
η	0.140792	$0.140790 \pm 3e-6$

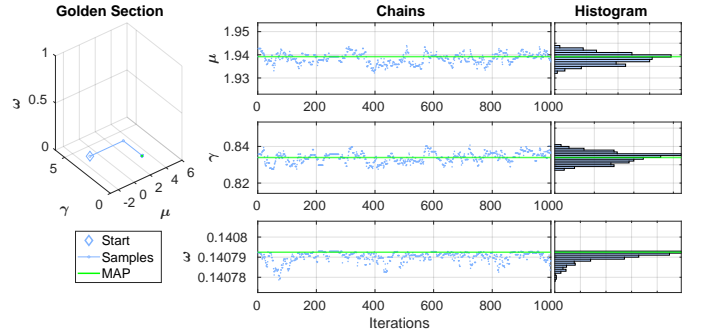


Fig. 8: MAP, chains and histograms on real data.

VII. CONCLUSION

The proposed approach effectively addresses the challenge of developing a probabilistic model for image processing that (1) enforces the positivity constraint, (2) controls the power spectral density, and (3) is explicitly defined. The model uses a positive-valued white field to ensure positivity, with correlation introduced through low-pass filtering, interpreted as a variable transformation to derive the prior's partition function. This framework offers flexibility in density modelling, enabling efficient Bayesian inference for parameter estimation. It lays the groundwork for fully self-supervised image deconvolution under the positivity constraint in future work, with careful qualitative and quantitative analysis of the constraint.

Future research will focus on refining the model by exploring alternative probability distributions and filtering techniques. Additionally, advanced sampling methods, such as Langevin [19], mirror Langevin [20], Fisher-Langevin algorithms [21], and Hamiltonian-based proposals [22], will be considered to extend the approach to a fully self-supervised inversion method for deconvolution, where the image itself becomes part of the estimation process. Contributions from [23] and [24] should also be considered.

REFERENCES

- [1] F. Orieux, J.-F. Giovannelli, and T. Rodet, "Bayesian estimation of regularization and point spread function parameters for wiener-hunt deconvolution," *J. Opt. Soc. Am. A*, vol. 27, no. 7, pp. 1593–1607, Jul 2010. [Online]. Available: <https://opg.optica.org/josaa/abstract.cfm?URI=josaa-27-7-1593>
- [2] J. G. Nagy and Z. Strakos, "Enforcing nonnegativity in image reconstruction algorithms," in *Mathematical Modeling, Estimation, and Imaging*, vol. 4121, International Society for Optics and Photonics. SPIE, 2000, pp. 182 – 190.
- [3] V. S. Reddy, "Development of high resolution system for stellar imaging," Ph.D. dissertation, University of Calcutta, January 2021, corrected Copy. [Online]. Available: <https://azpdf.net/document/qvl84xpl-development-of-high-resolution-system-for-stellar-imaging.html>
- [4] I. M. De la Torre, M. del Socorro Hernández Montes, J. M. Flores-Moreno, and F. M. Santoyo, "Laser speckle based digital optical methods in structural mechanics: A review," *Optics and Lasers in Engineering*, vol. 87, pp. 32–58, 2016.
- [5] D. Higdon, J. Bowshe, V. Johnson, T. Turkington, D. Gilland, and R. Jaszcak, "Fully Bayesian estimation of Gibbs hyperparameters for emission computed tomography data," *IEEE Transactions on Medical Imaging*, vol. 16, no. 5, pp. 516–526, 1997.
- [6] J.-F. Giovannelli, "Unsupervised bayesian convex deconvolution based on a field with an explicit partition function," *IEEE Transactions on Image Processing*, vol. 17, no. 1, p. 16–26, Jan. 2008. [Online]. Available: <http://dx.doi.org/10.1109/TIP.2007.911819>
- [7] E. Oti, M. Olusola, and F. Eze, "A study of properties and applications of Gamma distribution," *African Journal of Mathematics and Statistics Studies*, vol. 4, no. 2, pp. 52–65, July 2021.
- [8] F. Mainardi, "Lévy stable distributions in the theory of probability," Lecture Notes on Mathematical Physics, Department of Physics, University of Bologna, May 2007.
- [9] W. Horrace, "Moments of the truncated normal distribution," *Journal of Productivity Analysis*, vol. 43, pp. 133–138, 2015.
- [10] P. D. Lax, "Change of variables in multiple integrals," *The American Mathematical Monthly*, vol. 106, no. 6, pp. 497–501, July 1999.
- [11] S. Martucci and R. Mersereau, "New approaches to block filtering of images using symmetric convolution and the DST or DCT," in *1993 IEEE International Symposium on Circuits and Systems*, 1993, pp. 259–262 vol.1.
- [12] P. J. Davis, *Circulant Matrices*, 2nd ed. New York: Chelsea Publishing, 1979, pp. 184–191.
- [13] V. Mazet, D. Brie, and J. Idier, "Simulation of positive normal variables using several proposal distributions," in *IEEE Workshop Statistical Signal Processing*, July 2005, pp. 37–42.
- [14] N. Chopin, "Fast simulation of truncated gaussian distributions," *Statistics and Computing*, vol. 21, no. 2, p. 275–288, Jan. 2010. [Online]. Available: <http://dx.doi.org/10.1007/s11222-009-9168-1>
- [15] J. Idier, *Bayesian Approach to Inverse Problems*. ISTE Ltd and John Wiley & Sons Inc, Apr 2008.
- [16] S. Chib and E. Greenberg, "Understanding the Metropolis-Hastings algorithm," *The American Statistician*, vol. 49, no. 4, pp. 327–335, Nov. 1995.
- [17] G. Sandhya Rani, S. Jayan, and K. V. Nagaraja, "An extension of golden section algorithm for n-variable functions with matlab code," *IOP Conference Series: Materials Science and Engineering*, vol. 577, no. 1, p. 012175, nov 2019. [Online]. Available: <https://dx.doi.org/10.1088/1757-899X/577/1/012175>
- [18] European Southern Observatory (ESO), "The horsehead nebula (eso1839i)," 2018, image published by ESO. [Online]. Available: <https://www.eso.org/public/images/eso1839i/>
- [19] A. Durmus, S. Majewski, and B. Miasojedow, "Analysis of Langevin Monte Carlo via convex optimization," *Journal of Machine Learning Research*, vol. 20, no. 73, pp. 1–46, Feb. 2019.
- [20] K. S. Zhang, G. Peyré, J. Fadili, and M. Pereyra, "Wasserstein control of mirror langevin Monte Carlo," in *Proceedings of Thirty Third Conference on Learning Theory*, vol. 125, July 2020, pp. 3814–3841.
- [21] M. Titsias, "Optimal preconditioning and Fisher adaptive Langevin sampling," *Advances in Neural Information Processing Systems*, vol. 36, pp. 29 449–29 460, Dec. 2023.
- [22] F. Septier and P. Gareth, "Langevin and Hamiltonian based sequential MCMC for efficient bayesian filtering in high-dimensional spaces," *IEEE Journal of Selected Topics in Signal Processing*, vol. 10, no. 2, pp. 312–327, 2015.
- [23] J. Bardsley and P. Hansen, "MCMC algorithms for computational UQ of nonnegativity constrained linear inverse problems," *SIAM Journal on Scientific Computing*, vol. 42, no. 2, pp. A1269–A1288, 2020.
- [24] M. Amrouche, H. Carfantan, and J. Idier, "A partially collapsed Gibbs sampler for unsupervised nonnegative sparse signal restoration," in *IEEE International Conference on Acoustics, Speech and Signal Processing*, 2021, pp. 5519–5523.